JACS Au
AN OPEN ACCESS JOURNAL OF THE AMERICAN CHEMICAL SOCIETY

pubs.acs.org/jacsau
Article

Characterizing the Membrane Assembly of ASGPR Related to Mediated Endocytosis Using TriGalNAc-Probe-Based Super-Resolution Imaging

Junling Chen,*[,‖] Jiaqi Wang,[‖] Binglin Sui, Pengwei Jiang, Xumin Wang, Hongda Wang,* and Feng Liang*

Cite This: JACS Au 2025, 5, 2246−2256

Read Online

ACCESS | Metrics & More | Article Recommendations | Supporting Information

ABSTRACT: The asialoglycoprotein receptor (ASGPR) is a promising therapeutic target for drug delivery systems in hepatocellular carcinoma (HCC), exhibiting high affinity for specific carbohydrate residues and overexpression on malignant hepatic cells. However, their functional mechanisms remain poorly resolved at the single molecule level, hindering the rational optimization of ASGPR-targeted drug delivery systems. Here, we developed a trivalent *N*-acetylgalactosamine (TriGalNAc)-functionalized ligand probe leveraging high affinity to enable the nanoscale visualization of ASGPR organization and trafficking via super-resolution imaging. Fixed cell imaging revealed pronounced clustering patterns of the ASGPR on HCC membranes. In live cell experiments, we observed the distribution changes of residual ASGPR and returned ASGPR on the membrane during endocytosis, identifying protein clusters as key functional platforms for mediated ligand uptake. Additionally, comparisons with ligand probe binding under varying cell states confirmed that ASGPR aggregation degree correlates with its ligand-binding capacity. Strikingly, disruption of membrane carbohydrate cross-linking dispersed ASGPR clusters and attenuated ligand binding. These findings resolve the nanoscale assembly of ASGPR in HCC and unveil clustering-dependent ligand-binding regulation, advancing a fundamental understanding of ASGPR biology while providing new insights to refine receptor-targeted therapeutics.

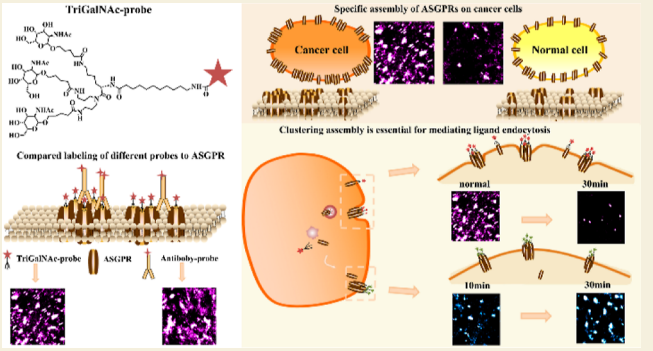

KEYWORDS: *asialoglycoprotein receptor assembly, ligand-probe labeling, super-resolution microscopy, ASGPR-mediated endocytosis*

The asialoglycoprotein receptor (ASGPR), a hepatic lectin receptor, has gained significant attention as a promising target for the development of novel drug delivery systems to enhance therapeutic efficacy and minimize side effects due to its specific binding to carbohydrate residues such as galactose (Gal) and *N*-acetylgalactosamine (*N*-GalNAc).[1−3] Furthermore, aberrant ASGPR expression is associated with various hepatic diseases, including hepatitis and hepatocellular carcinoma, underscoring its clinical significance for early diagnosis and therapeutic development. For deep understanding of ASGPR in mediated endocytosis, recent research has primarily focused on ASGPR's specificity and affinity for various carbohydrate ligands,[4] elucidating the pathways and mechanisms of ligand internalization and engineering novel nanodelivery systems.[5−8] However, there remains a lack of fine-scale observation of ASGPR at the in situ single-molecule level as well as deeper biological details in ASGPR-mediated ligand endocytosis.

The spatial localization and assembly of biomolecules, particularly membrane molecules, are intrinsically linked to their biological functions.[9] High-definition and accurate observation of biomolecules allows for the in situ determination of spatial distribution and assembly, offering new perspectives for a comprehensive understanding of their functions.[10] Revealing the fine changes in molecular spatial information aids in elucidating alterations in their biological functions.[11,12] Direct observation of the binding interactions between ASGPR and the ligand will offer valuable insights into their binding characteristics. Moreover, precise localization of ASGPR within live cells facilitates the understanding of its intracellular transport processes. To achieve these objectives, high-resolution imaging techniques and accurate labeling methods are essential for acquiring detailed single-molecule biological information on ASGPR.

Received: February 21, 2025
Revised: April 29, 2025
Accepted: April 30, 2025
Published: May 8, 2025

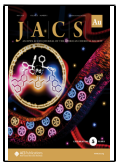

https://doi.org/10.1021/jacsau.5c00193
JACS Au 2025, 5, 2246−2256

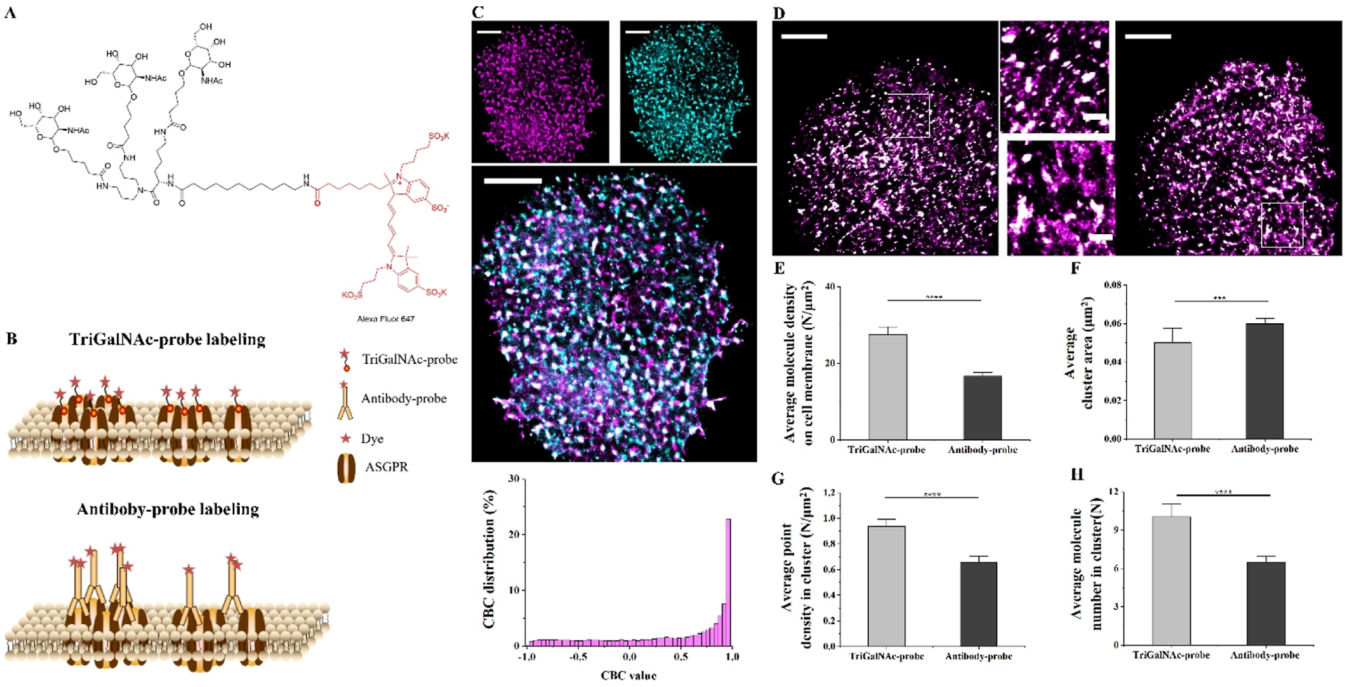

Figure 1. Synthesis and labeling properties of the TriGalNAc-probe. (A) Structural formula of TriGalNAc-Alexa647; (B) schematic diagram of different labeling features of the TriGalNAc-probe and antibody-probe for ASGPR on the cell membrane; (C) reconstructed dSTORM images of ASGPRs on the fixed Hep-G2 cell membranes by TriGalNAc-Alexa647 labeling (in Magenta) and antibody-Alexa532 labeling (in Cyan), and the distribution histogram of V_{CBC} in CBC analysis; (D) reconstructed dSTORM images of ASGPR on the fixed Hep-G2 cell membranes by TriGalNAc-Alexa647 labeling (left) or antibody-Alexa647 labeling (right); (E−H) comparison histograms of the average molecule density on the cell membrane (E), average cluster area (F), average point density in the cluster (G), and average molecule number in cluster (H) from TriGalNAc probe labeling (in gray) and antibody-probe labeling (in black). All data are statistical results of more than ten cells from three independent experiments. The significant difference analyses were performed by the unpaired two-tailed *t*-test, with "***" meaning $P < 0.001$ and "****" meaning $P < 0.0001$. Scale bars are 5 μm in original images and are 500 nm in enlarged images.

Super-resolution fluorescence imaging techniques, particularly direct stochastic optical reconstruction microscopy (dSTORM), offer nanoscale resolution ideal for revealing biomolecular spatial information.[13−15] In recent years, fluorescent labeling tools that surpass traditional antibody probes have evolved to enhance the imaging resolution.[16,17] Small-molecule fluorescent probes, due to their size, specificity, ease of synthesis, and stability, have emerged as efficient labeling methods.[14,18]

Here, based on the high affinity of ASGPR with trivalent *N*-acetylgalactosamine (TriGalNAc),[19,20] we synthesized the TriGalNAc ligand probe for ASGPR. After confirming its binding specificity and labeling advantages in dSTORM imaging, we observed district aggregation distribution of ASGPR on HCC membranes. Through live-cell labeling, we uncovered a dynamic cycle of ASGPR clustering: disassembly during endocytosis and subsequent reassembly for further ligand internalization, suggesting that the clustering assembly of ASGPR may serve as a critical functional platform for mediated endocytosis. This clustering behavior was further confirmed to be functionally essential by finding that disruption of clathrin-mediated endocytosis or low-temperature treatment was revealed to attenuate ASGPR clustering and weaken ligand binding. Finally, free sialic acid (Sia) treatment and glycosidase F (PNGase F) treatment impaired ASGPR clustering and subsequent ligand internalization, indicating the cross-linking of membrane carbohydrates is vital for the formation of ASGPR clusters and finally affects ASGPR's function in mediated endocytosis. These findings not only provide new insights into the mechanism of ASGPR-mediated endocytosis but also offer valuable implications for the development of targeted drug delivery systems and cancer therapeutics. The TriGalNAc-based probe and super-resolution imaging approach established in this study present a powerful tool for further investigations of receptor dynamics and targeted therapy development.

MATERIALS AND METHODS

Sample Preparation for Single-Color dSTORM Imaging

For fixed cell imaging, cell-laden slides were fixed with 4% PFA for 20 min at room temperature. After fixation, cells were washed with PBS, blocked with 3% BSA for 20 min at room temperature, and then stained with a 0.3 μM TriGalNAc probe for 10 min at room temperature in the dark or stained with antibody probes for 30 min. Wash 4 times with PBS. 50 μL of imaging buffer was dropped onto a 24 mm × 50 mm large slide. The imaging buffer contains the following: Tris (50 mM, pH 8.0), NaCl (10 mM), glucose (10% w/v), glucose oxidase (500 μg/mL, sigma), catalase (40 μg/mL, sigma), and β-mercaptoethanol (1% v/v, sigma). Then mount a small slide with cells onto a larger slide and seal it with nail polish.

Reagent Treatment

Cells were washed with PBS and treated with Pitstop2 or PNGase F or sialic acid for 20 min, then the samples were fixed and stained with TriGalNAc probes or antibody probes as described above, and the cell culture dish was placed directly at 4 °C during incubation at 4 °C, followed by fixation and sample preparation.

dSTORM Imaging

For dSTORM imaging, we used an inverted Nikon Ti-E microscope with an oil-immersion objective (100×, 1.49 NA, Nikon, Japan). The sample was imaged under the total internal reflection fluorescence

https://doi.org/10.1021/jacsau.5c00193
JACS Au 2025, 5, 2246−2256

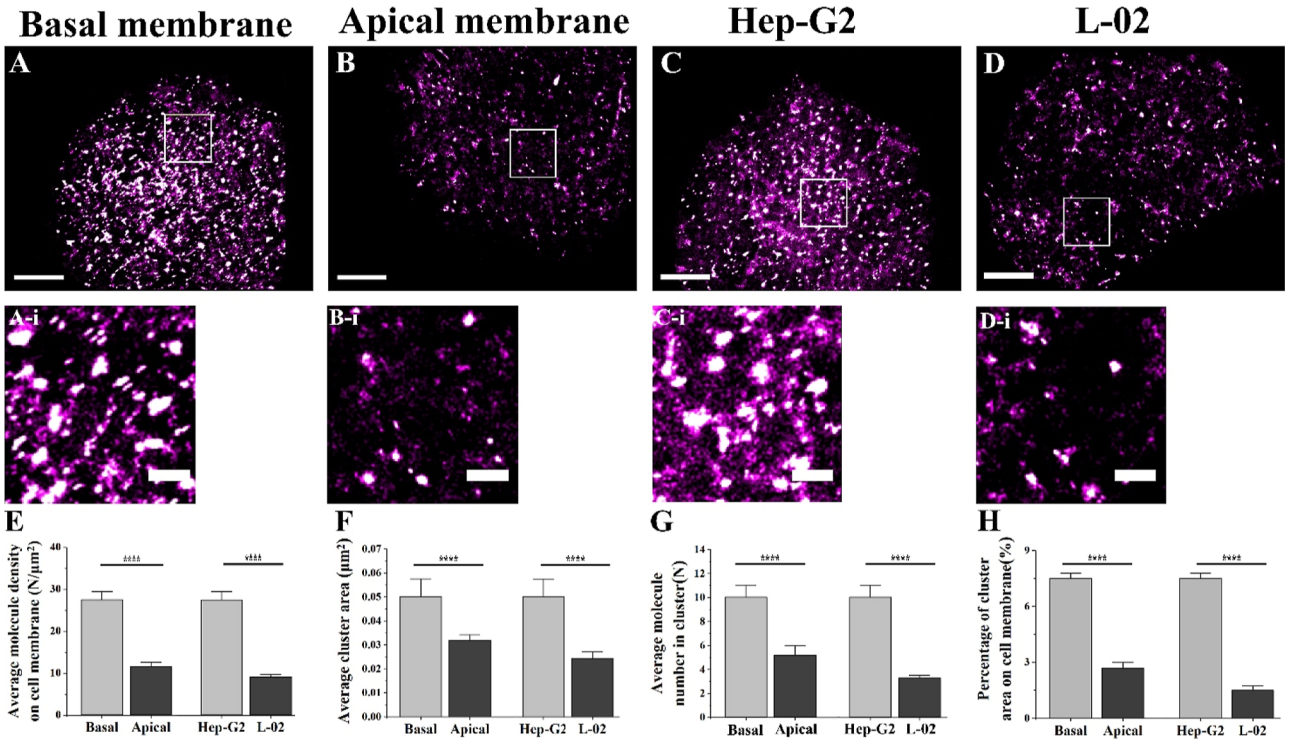

Figure 2. Comparison of dSTORM imaging of ASGPRs on different cell membranes by TriGalNAc-probe labeling. (A−C) Reconstructed dSTORM images of AS-GPRs on the fixed Hep-G2 basal membrane (A) and apical membrane (B) as well as on the basal membranes of Hep-G2 cell (C) and L-02 cell (D). (E−H) Corresponding compared histograms of the average molecule density on the membrane (E), average cluster area (F), average molecule number in cluster (G), and coverage percentage of clusters on the cell membrane (H). All data are statistical results of more than 10 cells from three independent experiments. The significant difference analyses were performed by the unpaired two-tailed *t*-test, with "****" meaning $P < 0.0001$. Scale bars are 5 μm in (A−D) and are 500 nm in enlarged images.

(TIRF) illuminating mode by adjusting the excitation inclination to maximize the signal-to-noise ratio. For single-color dSTORM imaging, a 532 nm laser was used for excitation. For dual-color dSTORM imaging, the sample was first imaged by using 639 nm laser illumination and then with 532 nm laser excitation. To prevent color crosstalk, two bandpass emission filters (FF01-565/133-25, FF02-675/67-25, Semrock) were added in addition to the conventional excitation filter, dichroic mirror, and emission filter set. In addition, the Nikon micro imaging device provides a complete focusing system (PFS) for real-time correction of *y*-axis focus drift. Finally, using Micro-Manager based on ImageJ (U.S. National Institutes of Health), we acquired 8000 raw frames with an EMCCD camera (IXON-L-897 Andor) at an exposure time of 20 ms.

Additional experimental procedures and data processing methods are detailed in the Supporting Information.

RESULTS AND DISCUSSION

Synthesis of the TriGalNAc-Probe and Demonstration of Its Labeling Characteristic

TriGalNAc is a saccharide molecule with three GalNAc antennae and has been reported to serve as a specific ligand that binds to ASGPR with high affinity.[4,21] Thus, we designed the small molecule fluorescent probe based on the TriGalNAc as the effective recognized unit for ASGPR. We select dityl-butyl (azanediylbis (propane-3,1-diyl)) dicarbamate as the start material, react it with an L-lysine derivative, and perform deprotection to give benzyl (*S*)-(6-amino-1-(bis(3-aminopropyl)amino)-1-oxohexan-2-yl)carbamate, which condensates with 5-(((2*R*,3*R*,4*R*,5*R*,6*R*)-3-acetamido-4,5-diacetoxy-6-(acetoxymethyl)tetrahydro-2*H*-pyran-2-yl)oxy)-pentanoic acid to give the Tri-GalNAc precursor 4. After deprotection and reaction with long chain acid to afford a reactive amino group, the dye molecule can be used to construct the TriGalNAc-probe. The chemical structural formula of TirGalNAc-Alexa647 is shown in Figure 1A, and the detailed synthetic route (Figure S1) and the corresponding ^{1}H NMR spectra of related compounds and LCMS (Figures S2 and S3) are shown in the Supporting Information. As shown in the schematic diagram (Figure 1B), when labeling ASGPRs on a cellular membrane, in comparison to antibody-probe labeling, the small volume of ligand-probe, one-to-one dye binding ratio, and no cross-linking effect can effectively reduce steric hindrance and linkage error. This allows for more accurate and high-density labeling of densely distributed ASGPR.

To examine the labeling specificity of this synthetic probe, we performed dual-color dSTORM imaging using TriGalNAc-Alexa647 probes (in Magenta) and antibody-Alexa532 probes (in Cyan). The imaging revealed nearly identical assembly patterns of ASGPR between the two labeling approaches (Figure 1C-upper). Quantitative assessment using coordinate-based colocalization (CBC) analysis, a standard method in super-resolution imaging,[22,23] demonstrated strong spatial correlation between the two probe types. The normalized CBC values (V_{CBC}), ranging from −1 (anticorrelation) to +1 (complete correlation), showed that 75% of the data points fell within the positive correlation range (0−1) (Figure 1C-below), indicating comparable specificity between the synthetic and antibody probes. Additionally, control experiments using ASGPR-negative cells (human red blood cells and human breast cancer cells MCF7 cells) showed minimal

https://doi.org/10.1021/jacsau.5c00193
JACS Au 2025, 5, 2246−2256

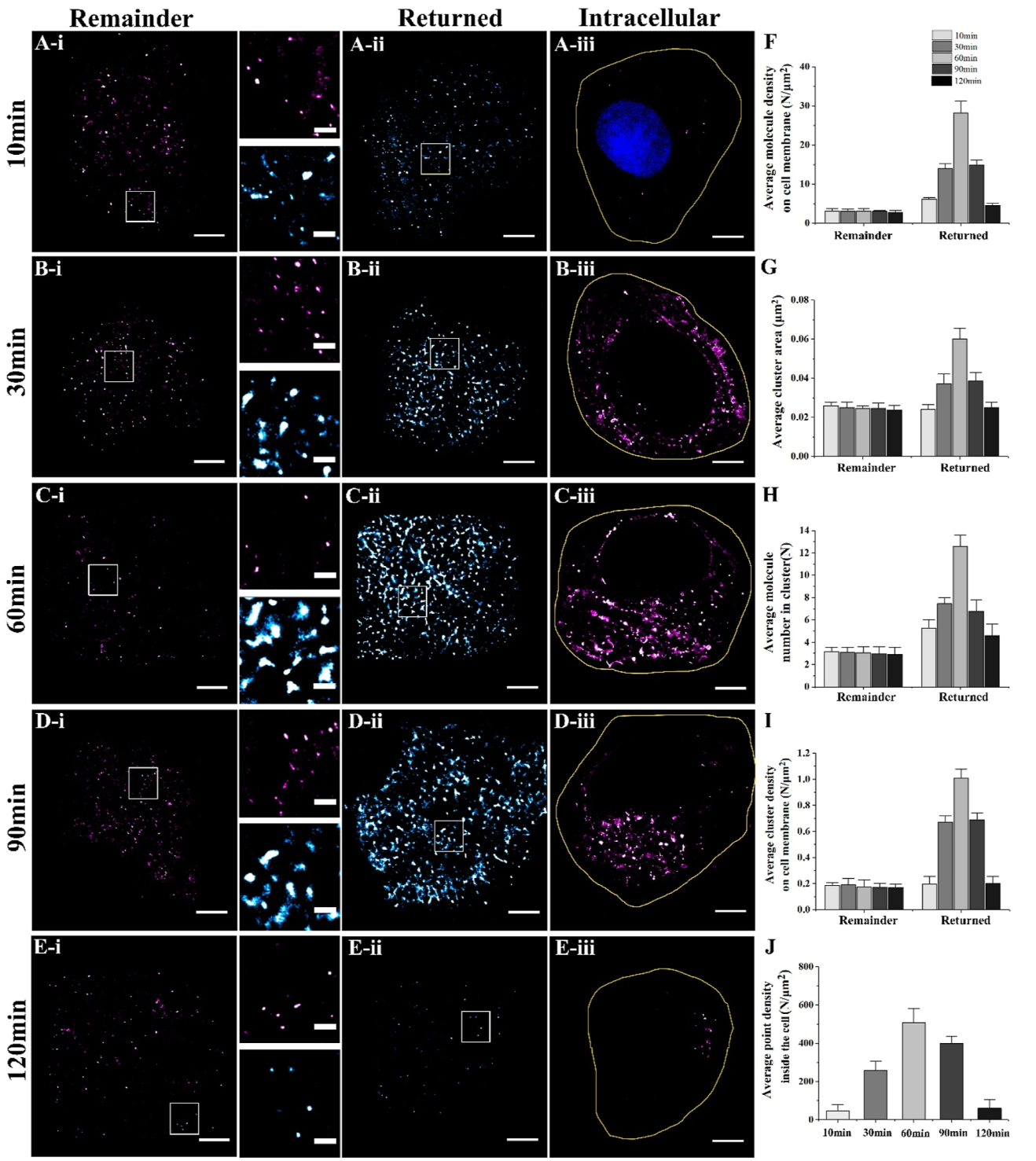

Figure 3. dSTORM imaging of remaining ASGPRs (i) and returned ASGPRs (ii) on the cell membrane and intracellular ASGPRs on the clearest focal plane of the nucleus (iii) under incubation with TriGalNAc-Alexa647 for 10 min (A), 30 min (B), 60 min (C), 90 min (D), and 120 min (E). (F–J) Compared histograms of the average molecule density on membrane (F), average cluster area (G), average molecule number in cluster (H), and average cluster density on the cell membrane (I) and the average point density inside the cells (J) from different incubation experiments. All data are statistical results of more than ten cells from three independent experiments. Scale bars are 5 μm in (A–E) and are 500 nm in enlarged images.

background fluorescence (Figure S4), confirming the probe's negligible nonspecific binding capacity.

To optimize the imaging conditions, we compared the imaging results at various labeling concentrations and ultimately established 0.3 μM as the optimal probe labeling concentration for Hep-G2 (Figure S5). Comparative dSTORM imaging from the TriGalNAc-probe (Figure 1D-left) and antibody-probe labeling (Figure 1D-right) displayed similar fluorescence intensity distributions and protein clustering patterns, but quantitative analysis of the average molecule density on the cell membrane demonstrated superior labeling density with the ligand probe, showing ~27.47

https://doi.org/10.1021/jacsau.5c00193
JACS Au 2025, 5, 2246–2256

molecules per μm^2 for the ligand probe vs ∼16.57 molecules per μm^2 for the antibody-probe (Figure 1E), revealing that our ligand probe outperformed conventional antibody-probes in labeling density. To further characterize the differences in protein assembly, we applied SR-Tesseler analysis, a common cluster analysis method for single molecule localization data,[24] to accurately and automatically extract the qualified clusters based on the local density of points (Figure S6). As observed from the results of TriGalNAc-probe labeling vs antibody-probe labeling, the average area of clusters was ∼0.051 μm^2 vs ∼0.064 μm^2 (Figure 1F) and the average point density in clusters was ∼0.92 points per 100 nm^2 vs ∼0.68 points per 100 nm^2 (Figure 1G). To further compare protein density and spatial organization within the cluster, semiquantitative data on protein number in cluster were normalized by fluorescence point counts against the average blinking frequency of individual probes, showing that the average number of molecules in the cluster was ∼10.03 vs ∼6.50 (Figure 1H). These data indicate that as a small molecule probe with a smaller linkage error and reduced steric hindrance, the TriGalNAc-probe enables more accurately present ASGPR distribution on cell membranes with a higher labeling density. Therefore, application of the TriGalNAc-probe can facilitate a high-quality spatial distribution morphology of ASGPR on the fixed cells.

Specific Assembly Patterns of ASGPR Related to Its Functional Efficiency on Various Cell Membranes

We further observed a striking polarity in the spatial organization of ASGPR across cell membranes by employing dSTORM imaging of fixed Hep-G2 cells labeled with TriGalNAc-Alexa647. A substantial amount of ASGPRs was found on the basal membrane, with high-intensity fluorescent points aggregating into large clusters (Figure 2A). In contrast, only a limited number of ASGPRs are located on the apical membrane, assembling sparsely into small protein domains (Figure 2B). The data of average molecule density on the membrane also demonstrated a pronounced basal membrane preference, with ∼27.47 molecules per μm^2 on the apical membrane and ∼11.52 molecules per μm^2 on the basal membrane (Figure 2E). With SR-Tesseler analysis (Figure S7), this polarized distribution was further characterized by distinct clustering patterns: basal membrane clusters exhibited larger average areas (∼0.050 μm^2 vs ∼0.032 μm^2) (Figure 2F), higher intracluster point densities (∼0.92 points per 100 nm^2 vs ∼0.67 points per 100 nm^2) (Figure S8), and greater molecular aggregation (∼10.03 vs ∼5.36 molecules per cluster) (Figure 2G). Average coverage percentage of clusters on the cell membrane also showed that most ASGPRs assembled into large clusters to form more significant coverage of cluster (∼7.5%) on the basal membrane than that (∼2.7%) on the apical membrane (Figure 2H). These findings suggest that ASGPR preferentially organizes into functional domains on the basal membrane, where enhanced clustering may facilitate more efficient ligand interactions through an increased local receptor density. This spatial organization likely represents an evolutionary adaptation to optimize ASGPR-mediated processes with basal membrane clusters serving as primary sites for ligand binding and signal transduction. The observed clustering patterns provide new insights into the assembly function relationship of ASGPR and its role in cellular signaling pathways.

Considering that ASGPR has been reported to be involved in the growth and invasion of hepatocellular carcinoma (HCC) cells,[21,25] we further revealed the specific assembly morphology of ASGPR associated with its dysfunction on HCC cells by comparing dSTORM imaging of normal liver cells (L-02 cells) and HCC cells (Hep-G2 cells). Most ASGPRs were observed to aggregate into markedly clustering distribution (Figure 2C) on the basal membrane of Hep-G2 cells, whereas ones on the L-02 cells mostly sparsely assembled into small domains (Figure 2D). Quantitative analysis demonstrated a striking increase in ASGPR expression on Hep-G2 cells (∼27.47 molecules per μm^2) compared to L-02 fundamental differences in spatial organization (Figure 2E); Hep-G2 cells exhibited larger cluster (∼0.050 μm^2 vs ∼0.022 μm^2) (Figure 2F), higher intracluster point density (∼0.92 per 100 nm^2 vs ∼0.63 points per 100 nm^2) (Figure S8), greater molecular aggregation (∼10.03 vs ∼3.35 molecules/cluster) (Figure 2G), and increased cluster coverage (∼7.50% vs ∼1.50%) (Figure 2H) compared to normal cells.

These results demonstrate that Hep-G2 cells show enhanced ASGPR expression not only by upregulating the total expression but also by reorganizing into more extensive, densely packed clusters. This transformation likely facilitates more efficient substrate clearance, potentially contributing to the tumor's ability to manipulate its microenvironment. The observed assembly changes in the ASGPR distribution may represent a critical adaptation in cancer progression, offering new insights into the relationship between receptor organization and cellular transformation in HCC. These assembly alterations could serve as potential biomarkers for cancer detection and therapeutic targeting.

Aggregated Assembly Pattern of ASGPR Facilitates Efficient Binding with Ligands

To further confirm that the clustering assembly of ASGPR serves as the primary functional domain for efficient ligand binding and endocytosis, we directly observed the live cells following incubation with ligand probes at 37 °C at different times. We observed a time-dependent reduction in the number of membrane-associated ASGPR clusters (Figure 3A−E(i)), with residual proteins primarily existing as monomers or small oligomers. Quantitative analysis revealed that compared with normal Hep-G2 cells, incubation with ligand-probes caused a significant decrease in membrane ASGPR density (from ∼27.47 to ∼3.09 (10 min), ∼3.11 (30 min), ∼3.07 (60 min), ∼3.02 (90 min), and ∼2.79 (120 min) molecules per μm^2) (Figure 3F), in cluster area (from ∼0.050 μm^2 to ∼0.026 μm^2 (10 min), ∼0.025 μm^2 (30 min), ∼0.025 μm^2 (60 min), ∼0.024 μm^2 (90 min), and ∼0.023 μm^2 (120 min)) (Figure 3G), and in intracluster molecule number (from ∼10.03 to ∼3.15 (10 min), ∼3.06 (30 min), ∼3.04 (60 min), ∼2.93 (90 min), and ∼2.90 (120 min)) (Figure 3H). We also noted that after endocytosis occurred, the distribution of residual ASGPR on the cell membrane was almost unchanged as prolonged incubation time, which was again reflected in the data of average cluster density on cell membrane (∼0.18 N per μm^2 (10 min), ∼0.19 N per μm^2 (30 min), ∼0.17 N per μm^2 (60 min), ∼0.17 N per μm^2 (90 min), and ∼0.17 N per μm^2 (120 min)) (Figure 3I). Additionally, we increased the incubated concentration of ligand probes and found similar imaging results, which eliminates the possibility that the relatively constant distribution of remaining ASGPRs over time was due to a lack of binding ligands in the extracellular environment

https://doi.org/10.1021/jacsau.5c00193
JACS Au 2025, 5, 2246−2256

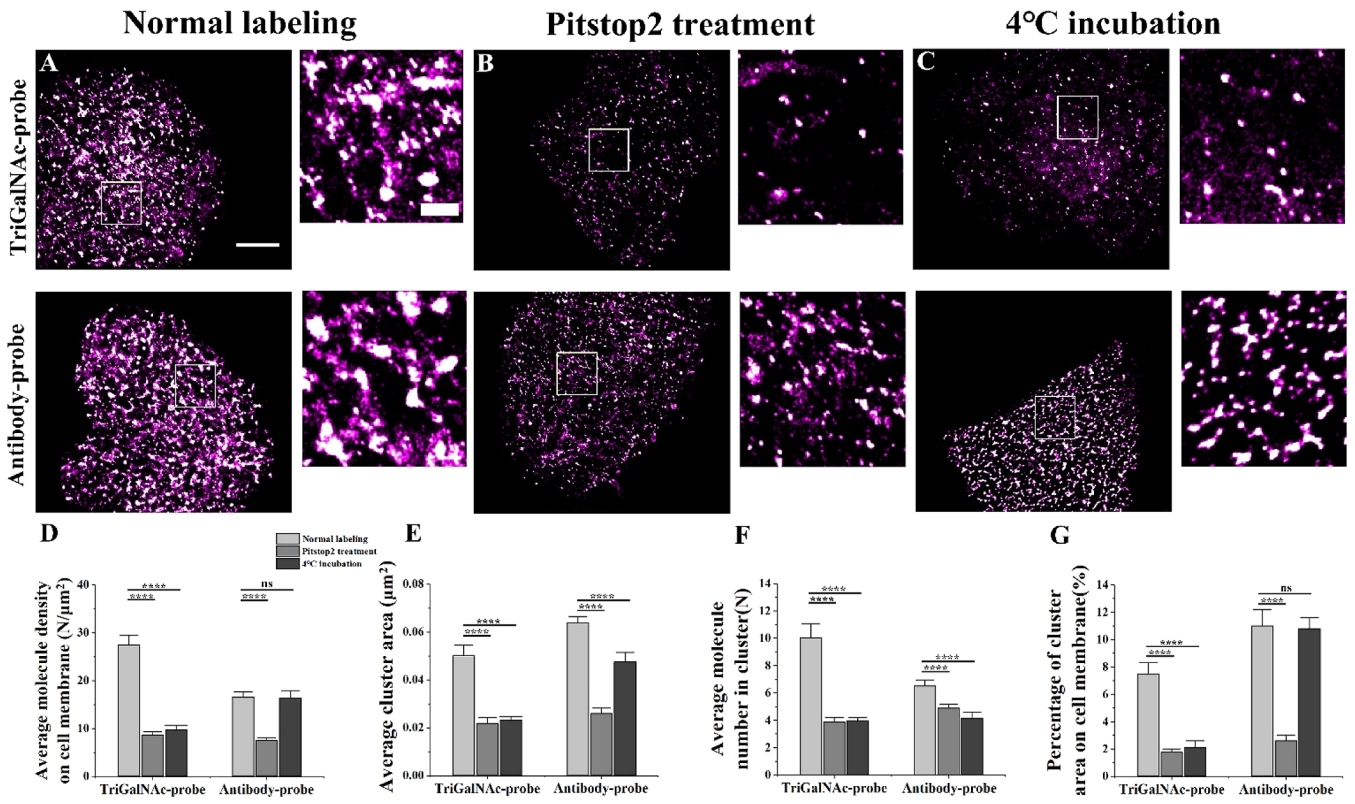

Figure 4. Corresponding distribution changes of ASGPRs on cells whose different endocytic activities were inhibited. (A−C) Reconstructed dSTORM images of ASGPRs on normal fixed cells (A), on cells treated by Pitstop2 (B), and on cells incubated at 4 °C for 20 min (C) from TriGalNAc-probe labeling (upper) and antibody-probe labeling (below). (D−G) Compared histograms of the average molecule density on the cell membrane (D), average cluster area (E), average molecule number in cluster (F), and percent-age of cluster area on the cell membrane (G) from different imaging conditions. All data are statistical results of more than 10 cells from three independent experiments. The significant difference analyses were performed by the unpaired two-tailed *t*-test, with "ns" meaning no significant difference, "****" meaning $P < 0.0001$. Scale bars are 5 μm in (A−C) and are 500 nm in enlarged images.

(Figure S9). These changes indicate that incubating live cells with ligand probes at 37 °C causes lots of ASGPR to participate in mediating the ligand's endocytosis, especially those in large and compact assembly patterns. Notably, the persistent presence of monomeric/oligomeric ASGPRs (2−4 proteins) suggests these forms are less active in endocytosis.

We also observed the distribution of ASGPRs returning to the cell membrane by using TriGalNAc-Alexa532 labeling after incubation. The dynamic redistribution of returned ASGPR followed a distinct pattern: initial sparse distribution gradually transitioned to pronounced clustering, peaking at 60 min before diminishing (Figure 3A−E(ii)). The statistical data showed that the average molecule densities on the membrane were ∼6.11 (10 min), ∼14.00 (30 min), ∼28.00 (60 min), ∼14.00 (90 min), and ∼4.50 (120 min) molecules per μm^2 (Figure 3F); the average cluster areas were ∼0.024 μm^2 (10 min), ∼0.037 μm^2 (30 min), ∼0.060 μm^2 (60 min), ∼0.038 μm^2 (90 min), and ∼0.025 μm^2 (120 min) (Figure 3G). Average molecule numbers in the cluster were ∼5.26 (10 min), ∼7.44 (30 min), ∼12.59 (60 min), ∼6.75 (90 min), and ∼4.57 (120 min) (Figure 3H); average cluster densities on the cell membrane were ∼0.19 per μm^2 (10 min), ∼0.67 per μm^2 (30 min), ∼1.00 per μm^2 (60 min), ∼0.69 per μm^2 (90 min), and ∼0.20 per μm^2 (120 min) (Figure 3I). This cyclical behavior, characterized by cluster reassembly and subsequent disassembly during endocytosis, strongly supports the functional importance of ASGPR clustering.

We also conducted intracellular imaging of fluorescent probes (Figure 3A(iii)−E(iii)) and observed a dynamic change in average point density inside cells, which increased from 45 to 258, peaked at 506, then decreased to 399, and finally dropped to 60 N per μm^2 (Figure 3J). This temporal progression revealed intracellular distribution changes of ligand-probes from peripheral to perinuclear localization, consistent with endocytic transport and subsequent degradation.

These findings demonstrate that ASGPR-mediated endocytosis is tightly regulated through cluster formation and disassembly. The large, dense clusters appear to function as high-efficiency endocytic platforms, while monomeric/oligomeric forms may represent an inactive reserve pool. This dynamic clustering behavior provides a mechanistic framework for understanding ASGPR's role in ligand internalization and suggests potential strategies for modulating its activity in therapeutic contexts.

Impact of Cellular Endocytic Activity on the Assembly Pattern of ASGPR and Its Ability to Bind Ligands

To elucidate the relationship among ASGPR clustering, ligand binding, and endocytosis efficiency, we systematically perturbed the endocytic pathway and quantified the changes in ASGPR organization and function. Compared with normal fixed cells (Figure 4A-upper), inhibition of clathrin-mediated endocytosis using Pitstop[26,27] resulted in dramatic reorganization of ASGPR (Figure 4B-upper), with molecule density on

https://doi.org/10.1021/jacsau.5c00193
JACS Au 2025, 5, 2246−2256

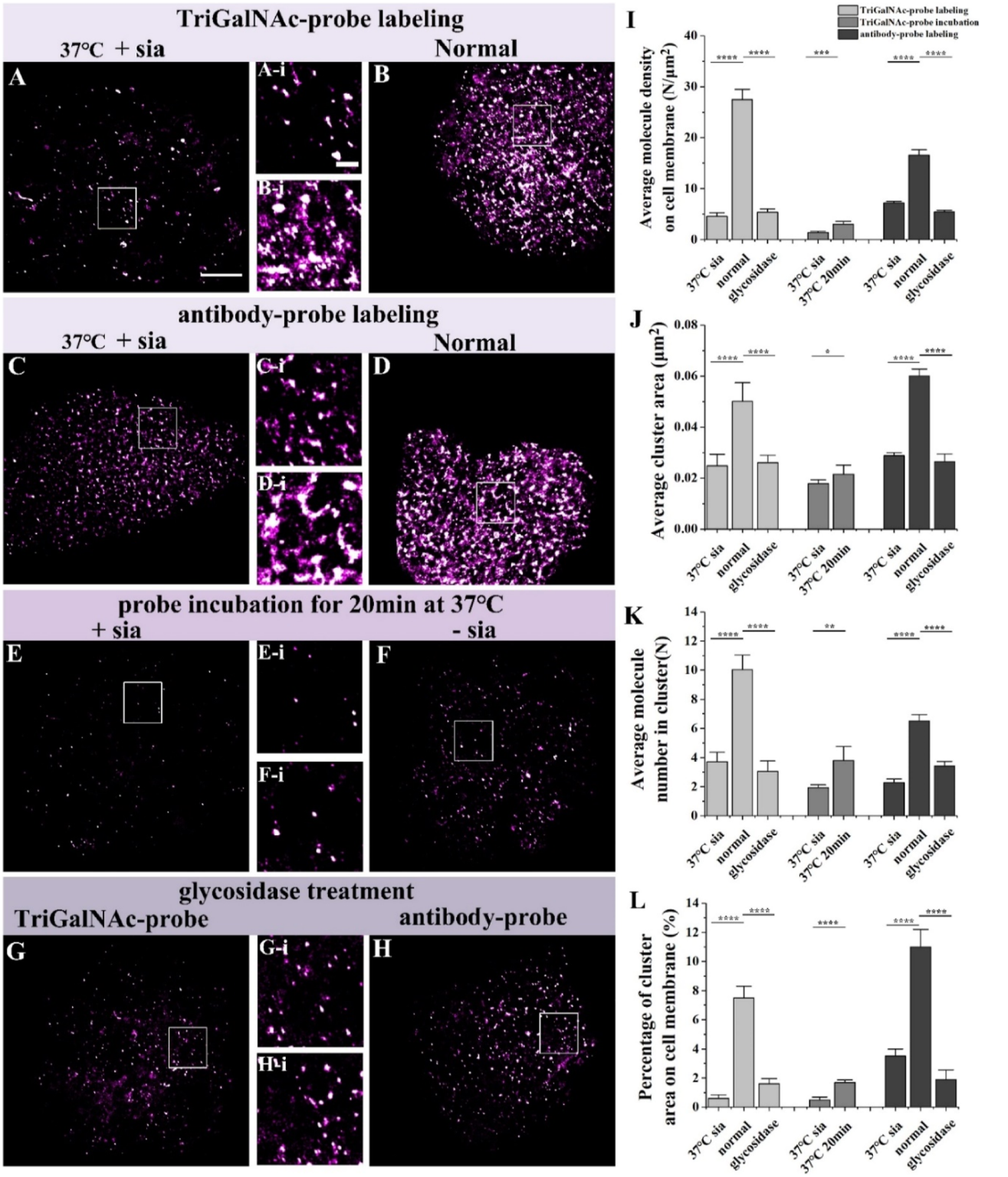

Figure 5. (A–D) dSTORM imaging of Hep-G2 cells preincubated with free Sia (A,C) or not (B,D) at 37 °C for 20 min by ligand-probe labeling (A,B) or antibody-probe labeling (C,D). (E,F) dSTORM imaging of Hep-G2 cells incubated with ligand-probes in the presence of free Sia (E) or not (F) at 37 °C for 20 min. (G,H) dSTORM imaging of Hep-G2 cells treated with PNGase F by ligand-probe labeling (G) or antibody-probe labeling (H). (I–L) Compared histograms of the average molecule density on the cell membrane (I), average cluster area (J), average molecules number in cluster (K), and percentage of clusters area on cell membrane (L) from different imaging conditions. All data are statistical results of more than 10 cells from three independent experiments. The significant difference analyses were performed by the unpaired two-tailed *t*-test, with "ns" meaning no significant difference, "*" meaning $P < 0.05$, "**" meaning $P < 0.01$, "***" meaning $P < 0.001$ "****" meaning $P < 0.0001$. Scale bars are 5 μm in (A–H), and are 500 nm in enlarged images.

https://doi.org/10.1021/jacsau.5c00193
JACS Au 2025, 5, 2246–2256

treated membranes decreasing by 68.80% (Figure 4D), cluster size reducing by 58.00% (Figure 4E), intracluster molecule number diminishing by 61.52% (Figure 4F), and cluster coverage declining by 68% (Figure 4G). The corresponding intracellular imaging revealed nearly no fluorescent point inside the cells (Figure S10), confirming that clathrin-mediated endocytosis is indeed the principal pathway for ligand internalization via ASGPR. These findings suggest that clathrin not only facilitates endocytosis but also promotes the formation of functional ASGPR clusters, creating a positive feedback loop that enhances ligand binding and internalization.

Furthermore, the corresponding imaging from antibody-probe labeling also displayed a large reduction in both the distribution amount and clustering morphology of ASGPRs on the treated membranes (Figure 4B-below) compared to imaging on normal fixed cells (Figure 4A-below). Molecule density on treated membrane reduced by 55.16% (Figure 4D); cluster area decreased by 66.67% (Figure 4E); protein number per cluster declined by 24.77% (Figure 4F); and cluster coverage percentage diminished by 76.36% (Figure 4G). These similar imaging results from two types of probe labeling suggest that clathrin is involved in the ASGPR-mediated endocytosis by facilitating remarkable aggregation of ASGPR into clusters, thereby enhancing its ability to bind with ligands.

We further investigated the binding changes of ASGPRs to ligands in cells subjected at 4 °C, which was reported to restrict cellular endocytosis by energy limitation.[28,29] There was nearly no fluorescent spot distributed inside the cells incubated with ligand probes at 4 °C (Figure S11), indicating that cells at 4 °C did not undergo ASGPR-mediated ligand endocytosis. The clustering distribution of fluorescent points on the membrane was significantly reduced, leaving only small domains or individual points (Figure 4C-upper). Molecule density on treated membrane reduced by 64.58% (Figure 4D), cluster area decreased by 54.00% (Figure 4E), protein number in the cluster declined by 60.52% (Figure 4F), and coverage percentage of clusters shrunk by 72.00% (Figure 4G). These results indicate that when cellular endocytosis is inhibited at 4 °C, the binding amount of ASGPR to ligand probes become significantly weaker. Moreover, similar imaging results of fixed cells labeled with ligand-probes at various temperatures (4 °C, room temperature of ∼25 and 37 °C) confirmed that these changes resulted from inhibited endocytosis rather than direct temperature effects on ligand binding (Figure S12).

Furthermore, the corresponding antibody-probe labeling provided complementary insights. Compared to normal cells, the intensity of fluorescent dots on the cell surface remained relatively unchanged (Figure 4C-below), as observed from the average molecule density on the membrane (∼16.35 vs ∼16.57 molecules per μm^2) (Figure 4D) and the average cluster coverage (∼10.80% vs ∼11.00%) (Figure 4G). However, detailed assembly patterns were markedly altered, as shown by the average cluster area decreasing by ∼25.40% (Figure 4E) and the average molecule number in the cluster declining by ∼36.15% (Figure 4F). This dissociation between total protein density and cluster organization suggests that energy restriction primarily affects ASGPR's ability to form functional clusters rather than its membrane association.

These findings establish a clear mechanistic link between the ASGPR clustering and its functional capacity. This integrated view of ASGPR organization and function provides new insights into the regulation of receptor-mediated endocytosis and suggests potential strategies for modulating this process in therapeutic contexts.

Additionally, these results also demonstrate that TriGalNAc-probes can be used to visually assess ligand binding to ASGPR by examining the distribution of fluorescent points, in addition to as a specific fluorescent probe to display the real ASGPR distribution under normal labeling conditions. To exclude that the sparse distribution of ASGPRs on L-02 cells may be caused by weak binding between ligand probes with ASGPRs, we compared the imaging of fixed L-02 cells labeled with antibody-probes and ligand probes. Similar imaging results showed that the two labeling applications of ligand probes were not conflicting (Figure S13).

Effect of Assembly Change of ASGPR on Its Binding to Ligand and Subsequent Mediated Endocytic Activity

About the assembly mechanism of ASGPR, we hypothesize that, as a membrane lectin receptor, the clustering distribution of ASGPRs may result from its cross-linking with membrane carbohydrate molecules. Intact Sia residues on the receptor were revealed as a requirement for the initial binding.[30] Here, we examined whether Sia residues were involved in the formation of ASGPR clusters and whether assembly changes of ASGPRs alter the binding with ligands and subsequent endocytic activity. Treatment of live cells with free Sia resulted in a dramatic reorganization of ASGPR (Figure 5A) compared with that on normal cells (Figure 5B), reducing the molecule density on the membrane by 83.33% (Figure 5I), cluster area by 52.00% (Figure 5J), intracluster molecule number by 63.01% (Figure 5K), and cluster coverage by 92.00% (Figure 5L). These changes indicate that Sia treatment significantly weakens the binding of ASGPR to ligands, leaving the distribution of ASGPRs capable of binding with ligands in small domains or as scattered proteins.

The effects of Sia treatment were confirmed through complementary antibody labeling on treated cells (Figure 5C) and normal cells (Figure 5D), which showed similar reductions in total membrane-associated ASGPR (56.67%) (Figure 5I), cluster organization (55.56% decrease in cluster size) (Figure 5J), intracluster molecule number (64.92%) (Figure 5K), and cluster coverage (68.18%) (Figure 5L). This consistency across labeling methods demonstrates that Sia disruption affects both ASGPR's membrane association and its organizational state, ultimately weakening the binding ability of ASGPR to ligands.

To further elucidate the impact of Sia on the binding of ASGPR to ligands, we directly observed the binding between ASGPR and ligand probes on the cell membrane in the presence of Sia at 37 °C (Figure 5E) as well as the distribution of internalized ligand probes within the cell (Figure S14). We found that compared to normal incubation with ligand probes (Figure 5F), the presence of Sia resulted in a weaker distribution of fluorescent points on the cell membrane, with a decrease of 53.67% in the average molecule density on the membrane (Figure 5I), a reduction of 19.05% in the cluster size (Figure 5J), a diminution of 48.98% decrease in the average molecule number per cluster (Figure 5K), and a decrement of 70.59% in the cluster coverage (Figure 5L). Additionally, the intercellular imaging of endocytic ligand-probes also showed a reduced distribution of ligand-probes inside cell. These results once again confirmed that free Sia treatment could attenuate the binding of ASGPR to ligand and ultimately reduced the amount of endocytic ligands. We

https://doi.org/10.1021/jacsau.5c00193
JACS Au 2025, 5, 2246−2256

propose that free Sia may function as a competitive carbohydrate, inhibiting the cross-linking of membrane glyconjugates to form large clusters of ASGPRs, which results in the formation of dispersed small domains or individual proteins, and finally reduces the binding capacity of ASGPR to ligand probes.

Further mechanistic insights came from PNGase F treatment, which cleaves *N*-glycans from the glycoproteins. After treating Hep-G2 cells with PNGase F, we respectively employed ligand-probe labeling (Figure 5G) and antibody-probe labeling (Figure 5H) for dSTORM imaging to observe ASGPR distribution changes. We found that both imaging results displayed significant decreases in the distribution amount and aggregated assembly state. The comparative statistical results from ligand-probe labeling or antibody-probe labeling show that PNGase F treatment yielded 80.45% or 67.11% reduction in molecule density on the treated membrane (Figure 5I), 48.00% or 56.67% decrease in the cluster area (Figure 5J), 69.49% or 47.23% reduction in the molecule number per cluster (Figure 5K), and 78.67% or 82.73% decrease in the cluster coverage (Figure 5L). These results suggest that as a membrane glycoprotein, ASGPR assembly is indeed influenced by the cross-linking effect of membrane carbohydrate chains, which promotes the formation of large protein clusters to maintain high binding capacity to ligands.

These findings support a model in which ASGPR clustering is maintained through a network of carbohydrate-mediated interactions. The *N*-glycan scaffold, with its terminal Sia residues, appears to serve as an organizational platform that promotes the formation of functional ASGPR clusters. This carbohydrate-dependent clustering mechanism provides a potential regulatory point for modulating the ASGPR activity.

CONCLUSION

Our study provides comprehensive insights into the assembly function relationship of ASGPR, revealing its organization changes and functional regulation in receptor-mediated endocytosis. Through synthesizing and validating the TriGalNAc ligand-based fluorescent probe, we demonstrated that ASGPR formed functionally critical clusters on the HCC basal membrane, with these high-density assemblies serving as efficient platforms for ligand binding and internalization. Live-cell labeling captured the cyclical nature of ASGPR-mediated endocytosis: cluster disassembly during ligand internalization, followed by receptor recycling and cluster reassembly for subsequent rounds of endocytosis.

Functional perturbation experiments established a direct correlation between ASGPR clustering and endocytic efficiency. Inhibition of clathrin-mediated endocytosis or energy restriction through low-temperature treatment disrupted ASGPR clustering, reducing the ligand binding capacity and endocytic activity. These findings highlight the interdependence of ASGPR's organizational state, ligand-binding capability, and endocytic function.

Mechanistic studies revealed the critical role of membrane carbohydrates in maintaining functional ASGPR clusters. Both Sia competition and PNGase F mediated *N*-glycan cleavage disrupted ASGPR clustering and membrane density, leading to attenuated ligand binding. This carbohydrate-dependent clustering mechanism provides a potential regulatory point for modulating ASGPR activity with implications for therapeutic targeting.

In summary, these findings significantly advance our understanding of ASGPR-mediated endocytosis, revealing a dynamic cycle of cluster assembly and disassembly that optimizes receptor function. The demonstrated relationship between ASGPR organization and functional efficiency provides a new framework for understanding membrane receptor dynamics and offers critical insights into the development of targeted drug delivery systems. Our ligand-based probe, combined with super-resolution imaging, establishes a powerful platform for further investigations of receptor-mediated endocytosis and its therapeutic applications.

ASSOCIATED CONTENT

Data Availability Statement

The data underlying this study are available in the published article and its Supporting Information.

Supporting Information

The Supporting Information is available free of charge at https://pubs.acs.org/doi/10.1021/jacsau.5c00193.

NMR and MS data of all new compounds and additional dSTORM imagings and analysis (PDF)

AUTHOR INFORMATION

Corresponding Authors

Junling Chen − *School of Chemistry & Chemical Engineering, Wuhan University of Science and Technology, Wuhan, Hubei 430081, China*; Email: chenjunling@wust.edu.cn

Hongda Wang − *State Key Laboratory of Electroanalytical Chemistry, Changchun Institute of Applied Chemistry, Chinese Academy of Sciences, Changchun, Jilin 130022, China*; orcid.org/0000-0003-4266-9012; Email: hdwang@ciac.ac.cn

Feng Liang − *School of Chemistry & Chemical Engineering, Wuhan University of Science and Technology, Wuhan, Hubei 430081, China*; orcid.org/0000-0002-3974-2621; Email: feng_liang@whu.edu.cn

Authors

Jiaqi Wang − *School of Chemistry & Chemical Engineering, Wuhan University of Science and Technology, Wuhan, Hubei 430081, China*

Binglin Sui − *College of Chemical Engineering and Environmental Chemistry, Weifang University, Weifang 261061, China*

Pengwei Jiang − *School of Chemistry & Chemical Engineering, Wuhan University of Science and Technology, Wuhan, Hubei 430081, China*

Xumin Wang − *School of Chemistry & Chemical Engineering, Wuhan University of Science and Technology, Wuhan, Hubei 430081, China*

Complete contact information is available at: https://pubs.acs.org/10.1021/jacsau.5c00193

Author Contributions

‖The manuscript was finished through contributions of all authors. All authors have given approval to the final version of the manuscript. J.C. and F.L. conceived the initial idea for this research. J.W. and J.C. performed the main experiments and data analysis; B.S. and P.J. analyzed parts of data; X.W. cultured cells; J.C. and J.W. wrote the manuscript; H.W. and F.L. provided the discussion and revised the manuscript. J.C.

https://doi.org/10.1021/jacsau.5c00193
JACS Au 2025, 5, 2246−2256

directed the whole research and revised manuscript. All authors declare no conflict of interest.

Notes

The authors declare no competing financial interest.

■ ACKNOWLEDGMENTS

We acknowledge the financial support from the Natural Science Foundation of Hubei Province (no. 2023AFB595 for J.C.); the National Natural Science Foundation of China (no. 22150003, 21721003 to H.W., no. 21807083 to J.C.); Research and Development Program of Scientific Instruments and Equipment of Chinese Academy of Sciences (no. ZDKYYQ20220005 to H.W.); Key-Area Research and Development Program of Guangdong Province (no. 2022B303040003 to H.W.); Provincial College Student's Innovation and Entrepreneurship Training Program (no. S202310488107 to J.C.); and Doctoral Research Start-up Fund of Weifang University (no. 2024BS17 to B.S.).

■ REFERENCES

(1) Zhang, X.; Chen, Y.; Li, X.; Xu, H.; Yang, J.; Wang, C.; Zhang, C.; Deng, Y.; Lu, A.; Zheng, C.; et al. Carrier-free self-assembled nanomedicine based on celastrol and galactose for targeting therapy of hepatocellular carcinoma via inducing ferroptosis. *Eur. J. Med. Chem.* **2024**, *267*, 116183.

(2) Zhang, Y.; Zhang, X.; Zeng, C.; Li, B.; Zhang, C.; Li, W.; Hou, X.; Dong, Y. Targeted delivery of atorvastatin via asialoglycoprotein receptor (ASGPR). *Bioorg. Med. Chem.* **2019**, *27* (11), 2187−2191.

(3) Petrov, R. A.; Mefedova, S. R.; Yamansarov, E. Y.; Maklakova, S. Y.; Grishin, D. A.; Lopatukhina, E. V.; Burenina, O. Y.; Lopukhov, A. V.; Kovalev, S. V.; Timchenko, Y. V.; et al. New Small-molecule Glycoconjugates of docetaxel and GalNAc for targeted delivery to hepatocellular carcinoma. *Mol. Pharm.* **2020**, *18* (1), 461−468.

(4) Reshitko, G. S.; Yamansarov, E. Y.; Evteev, S. A.; Lopatukhina, E. V.; Shkil', D. O.; Saltykova, I. V.; Lopukhov, A. V.; Kovalev, S. V.; Lobov, A. N.; Kislyakov, I. V.; et al. Synthesis and evaluation of new trivalent ligands for hepatocyte targeting via the asialoglycoprotein receptor. *Bioconjugate Chem.* **2020**, *31* (5), 1313−1319.

(5) Bovenschen, N.; Rijken, D. C.; Havekes, L. M.; Van Vlijmen, B. J. M.; Mertens, K. The B domain of coagulation factor VIII interacts with the asialoglycoprotein receptor. *J. Thromb. Haemostasis* **2005**, *3* (6), 1257−1265.

(6) Zhang, X.; Ng, H. L. H.; Lu, A.; Lin, C.; Zhou, L.; Lin, G.; Zhang, Y.; Yang, Z.; Zhang, H. Drug delivery system targeting advanced hepatocellular carcinoma: current and future. *Nanomed. Nanotechnol. Biol. Med.* **2016**, *12* (4), 853−869.

(7) Poelstra, K.; Prakash, J.; Beljaars, L. Drug targeting to the diseased liver. *J. Controlled Release* **2012**, *161* (2), 188−197.

(8) Zhao, R.; Li, T.; Zheng, G.; Jiang, K.; Fan, L.; Shao, J. Simultaneous inhibition of growth and metastasis of hepatocellular carcinoma by co-delivery of ursolic acid and sorafenib using lactobionic acid modified and pH-sensitive chitosan-conjugated mesoporous silica nanocomplex. *Biomaterials* **2017**, *143*, 1−16.

(9) Delcanale, P.; Alampi, M. M.; Mussini, A.; Fumarola, C.; Galetti, M.; Petronini, P. G.; Viappiani, C.; Bruno, S.; Abbruzzetti, S. A photoactive supramolecular complex targeting PD-L1 reveals a weak correlation between photoactivation efficiency and receptor expression levels in non-small-cell lung cancer tumor models. *Pharmaceutics* **2023**, *15* (12), 2776.

(10) Chen, S.; Wang, J.; Xin, B.; Yang, Y.; Ma, Y.; Zhou, Y.; Yuan, L.; Huang, Z.; Yuan, Q. Direct observation of nanoparticles within cells at subcellular levels by super-resolution fluorescence imaging. *Anal. Chem.* **2019**, *91* (9), 5747−5752.

(11) Ge, D.; Chen, J.; Zhao, Z.; Sui, B.; Liang, F.; Wang, H. Characterizing the function-related specific assembly pattern of matrix metalloproteinase-14 by dSTORM imaging. *Talanta* **2023**, *260*, 124523.

(12) Jing, Y.; Chen, J.; Zhou, L.; Sun, J.; Cai, M.; Shi, Y.; Tian, Y.; Gao, J.; Wang, H. Super-resolution imaging of cancer-associated carbohy-drates using aptamer probes. *Nanoscale* **2019**, *11* (31), 14879−14886.

(13) Virant, D.; Traenkle, B.; Maier, J.; Kaiser, P. D.; Bodenhöfer, M.; Schmees, C.; Vojnovic, I.; Pisak-Lukáts, B.; Endesfelder, U.; Rothbauer, U. A peptide tag-specific nanobody enables high-quality labeling for dSTORM imaging. *Nat. Commun.* **2018**, *9* (1), 930.

(14) Sui, B.; Chen, J.; Ge, D.; Liang, F.; Wang, H. Assembly characterization of human equilibrium nucleoside transporter 1 (hENT1) by inhibitor probe-based dSTORM imaging. *Anal. Chem.* **2023**, *95* (24), 9207−9218.

(15) Man, H.; Bian, H.; Zhang, X.; Wang, C.; Huang, Z.; Yan, Y.; Ye, Z.; Xiao, Y. Hybrid labeling system for dSTORM imaging of endoplasmic reticulum for uncovering ultrastructural transformations under stress conditions. *Biosens. Bioelectron.* **2021**, *189*, 113378.

(16) Chang, C. J. Introduction: fluorescent probes in biology. *Chem. Rev.* **2024**, *124* (21), 11639−11640.

(17) Wilson, Q. D.; Sletten, E. M. Engineering cyanine cyclizations for new fluorogenic probes. *Nat. Chem.* **2024**, *16* (1), 3−5.

(18) Wu, Q.; Cai, M.; Gao, J.; Zhao, T.; Xu, H.; Yan, Q.; Jing, Y.; Shi, Y.; Kang, C.; Liu, Y.; et al. Developing substrate-based small molecule fluorescent probes for super-resolution fluorescent imaging of various membrane transporters. *Nanoscale Horiz.* **2020**, *5* (3), 523−529.

(19) Mishra, A.; Castañeda, T. R.; Bader, E.; Elshorst, B.; Cummings, S.; Scherer, P.; Bangari, D. S.; Loewe, C.; Schreuder, H.; Pöverlein, C.; et al. Triantennary GalNAc molecular imaging probes for monitoring hepatocyte function in a rat model of nonalcoholic steatohepatitis. *Adv. Sci.* **2020**, *7* (24), 2002997.

(20) Holland, R. J.; Lam, K.; Ye, X.; Martin, A. D.; Wood, M. C.; Palmer, L.; Fraser, D.; McClintock, K.; Majeski, S.; Jarosz, A.; et al. Ligand conjugate SAR and enhanced delivery in NHP. *Mol. Ther.* **2021**, *29* (10), 2910−2919.

(21) Willoughby, J. L. S.; Chan, A.; Sehgal, A.; Butler, J. S.; Nair, J. K.; Racie, T.; Shulga-Morskaya, S.; Nguyen, T.; Qian, K.; Yucius, K.; et al. Evaluation of GalNAc-siRNA conjugate activity in pre-clinical animal models with reduced asialoglycoprotein receptor expression. *Mol. Ther.* **2018**, *26* (1), 105−114.

(22) Malkusch, S.; Endesfelder, U.; Mondry, J.; Gelléri, M.; Verveer, P. J.; Heilemann, M. Coordinate-based colocalization analysis of single-molecule localization microscopy data. *Histochem. Cell Biol.* **2011**, *137* (1), 1−10.

(23) Schnitzbauer, J.; Wang, Y.; Zhao, S.; Bakalar, M.; Nuwal, T.; Chen, B.; Huang, B. Correlation analysis framework for localization-based superresolution microscopy. *Proc. Natl. Acad. Sci. U.S.A.* **2018**, *115* (13), 3219−3224.

(24) Levet, F.; Hosy, E.; Kechkar, A.; Butler, C.; Beghin, A.; Choquet, D.; Sibarita, J. B. SR-Tesseler: a method to segment and quantify localization-based super-resolution microscopy data. *Nat. Methods* **2015**, *12* (11), 1065−1071.

(25) Rigopoulou, E. I.; Roggenbuck, D.; Smyk, D. S.; Liaskos, C.; Mytilinaiou, M. G.; Feist, E.; Conrad, K.; Bogdanos, D. P. Asialoglycoprotein receptor (ASGPR) as target auto-antigen in liver autoimmunity: Lost and found. *Autoimmun. Rev.* **2012**, *12* (2), 260−269.

(26) Smith, C. M.; Haucke, V.; McCluskey, A.; Robinson, P. J.; Chircop, M. Inhibition of clathrin by pitstop 2 activates the spindle assembly checkpoint and induces cell death in dividing HeLa cancer cells. *Mol. Cancer* **2013**, *12* (1), 4−15.

(27) Robertson, M. J.; Deane, F. M.; Stahlschmidt, W.; von Kleist, L.; Haucke, V.; Robinson, P. J.; McCluskey, A. Synthesis of the Pitstop family of clathrin inhibitors. *Nat. Protoc.* **2014**, *9* (7), 1592−1606.

(28) Letoha, A.; Hudák, A.; Bozsó, Z.; Vizler, C.; Veres, G.; Szilák, L.; Letoha, T. The nuclear localization signal of NF-κB p50 enters the

https://doi.org/10.1021/jacsau.5c00193
JACS Au 2025, 5, 2246−2256

cells via syndecan-mediated endocytosis and inhibits NF-κB activity. *Int. J. Pept. Res. Ther.* **2023**, *29* (5), 73.
(29) Ishii, M.; Fukuoka, Y.; Deguchi, S.; Otake, H.; Tanino, T.; Nagai, N. Energy-Dependent endocytosis is involved in the absorption of indomethacin nanoparticles in the small intestine. *Int. J. Mol. Sci.* **2019**, *20* (3), 476.
(30) Ho, M.; Chelly, J.; Carter, N.; Danek, A.; Crocker, P.; Monaco, A. P. Isolation of the gene for McLeod syn-drome that encodes a novel membrane transport protein. *Cell* **1994**, *77* (6), 869−880.

https://doi.org/10.1021/jacsau.5c00193
JACS Au 2025, 5, 2246−2256